

The Discontinuous Galerkin Method for the Multiscale Modeling of Dynamics of Crystalline Solids

Wei Wang*, Xiantao Li[†] and Chi-Wang Shu*

August 26, 2007

Abstract

We present a multiscale model for numerical simulation of dynamics of crystalline solids. The method couples nonlinear elastodynamics as the continuum description and molecular dynamics as another component at the atomic scale. The governing equations on the macroscale are solved by the discontinuous Galerkin method, which is built up with an appropriate local curl-free space to produce coherent displacement field. The constitutive data are based on the underlying atomistic model: it is either calibrated prior to the computation or obtained from molecular dynamics as the computation proceeds. The decision to use either the former or the latter is made locally for each cell based on suitable criteria.

Key words: discontinuous Galerkin method, multiscale model, dynamics of crystalline solids, molecular dynamics

*Division of Applied Mathematics, Brown University, Providence, RI 02912. E-mail: {wwang}, {shu}@dam.brown.edu. Research supported by ARO grant W911NF-04-1-0291 and NSF grant DMS-0510345.

[†]Department of Mathematics, Pennsylvania State University, University Park, PA 16802. E-mail: xli@math.psu.edu. Research supported by NSF grant DMS-0609610 and the Alfred P. Sloan Fellowship.

Report Documentation Page

Form Approved
OMB No. 0704-0188

Public reporting burden for the collection of information is estimated to average 1 hour per response, including the time for reviewing instructions, searching existing data sources, gathering and maintaining the data needed, and completing and reviewing the collection of information. Send comments regarding this burden estimate or any other aspect of this collection of information, including suggestions for reducing this burden, to Washington Headquarters Services, Directorate for Information Operations and Reports, 1215 Jefferson Davis Highway, Suite 1204, Arlington VA 22202-4302. Respondents should be aware that notwithstanding any other provision of law, no person shall be subject to a penalty for failing to comply with a collection of information if it does not display a currently valid OMB control number.

1. REPORT DATE 26 AUG 2007	2. REPORT TYPE	3. DATES COVERED 00-00-2007 to 00-00-2007			
4. TITLE AND SUBTITLE The Discontinuous Galerkin Method for the Multiscale Modeling of Dynamics of Crystalline Solids		5a. CONTRACT NUMBER			
		5b. GRANT NUMBER			
		5c. PROGRAM ELEMENT NUMBER			
6. AUTHOR(S)		5d. PROJECT NUMBER			
		5e. TASK NUMBER			
		5f. WORK UNIT NUMBER			
7. PERFORMING ORGANIZATION NAME(S) AND ADDRESS(ES) Brown University, Division of Applied Mathematics, Providence, RI, 02912		8. PERFORMING ORGANIZATION REPORT NUMBER			
9. SPONSORING/MONITORING AGENCY NAME(S) AND ADDRESS(ES)		10. SPONSOR/MONITOR'S ACRONYM(S)			
		11. SPONSOR/MONITOR'S REPORT NUMBER(S)			
12. DISTRIBUTION/AVAILABILITY STATEMENT Approved for public release; distribution unlimited					
13. SUPPLEMENTARY NOTES					
14. ABSTRACT We present a multiscale model for numerical simulation of dynamics of crystalline solids. The method couples nonlinear elastodynamics as the continuum description and molecular dynamics as another component at the atomic scale. The governing equations on the macroscale are solved by the discontinuous Galerkin method, which is built up with an appropriate local curl-free space to produce coherent displacement field. The constitutive data are based on the underlying atomistic model: it is either calibrated prior to the computation or obtained from molecular dynamics as the computation proceeds. The decision to use either the former or the latter is made locally for each cell based on suitable criteria.					
15. SUBJECT TERMS					
16. SECURITY CLASSIFICATION OF:			17. LIMITATION OF ABSTRACT	18. NUMBER OF PAGES	19a. NAME OF RESPONSIBLE PERSON
a. REPORT unclassified	b. ABSTRACT unclassified	c. THIS PAGE unclassified	Same as Report (SAR)	41	

1 Introduction

The conventional computational methods for solid mechanics have been primarily based on continuum models, where one uses a small number of variables, such as the strain and stress, to efficiently describe the mechanical properties. The quality of these continuum models depends heavily on the constitutive assumptions, which are usually obtained from experimental observations. On the other hand, atomistic models, such as molecular statistics and molecular dynamics (MD), which account for detailed crystal structure and atomic configurations, have been proven to be a useful methodology. However, to model a macroscale process, such atomistic systems are too large to fit in a realistic computation. Therefore, it is computationally advantageous to develop a hybrid model that includes both components. Multiscale methods that aim to bridge different scales have been an active area of interest. Recently developed methods in this class include, for instance, the quasicontinuum methods [44, 32], the Macro Atomistic Ab initio Dynamics method (MAAD) [2], the bridging scale method [47], the bridging domain methods [48], the heterogeneous multiscale method (HMM) [23, 36, 24], and the pseudo-spectral method [45]. The advantage of such concurrent methods is that the models can be refined as the computation proceeds.

This paper is concerned with the dynamics of elastic solids. We will use the framework of HMM [23, 36]. The main idea of HMM is to formulate both the atomistic and continuum models in terms of universal conservation laws, and the coupling is accomplished by ensemble averaging. The implementation of such method consists of three components,

1. a macro solver for the continuum model,
2. a micro solver to equilibrate the atomistic system locally to the appropriate ensemble,
3. an averaging procedure to obtain data that are needed in the continuum model.

The main advantage of this formalism is that one is able to use the macroscale equations to capture the elastic waves, and the microscale models are employed as a supplemental component to provide accurate constitutive data, thereby bypassing any empirical model for the equation of state.

The constitutive relation obtained from the atomistic models are typically nonlinear and temperature dependent. As a result, shock waves may

develop, which give rise to large strain and velocity gradients, posing a great challenge for numerical simulations. In addition suitable constraints have to be imposed to form a coherent displacement field. The problem is further complicated by the presence of defects, causing large local deformation and discontinuity in strain and displacement. To overcome these difficulties, we will make use of the discontinuous Galerkin (DG) method, a finite element method based on piecewise polynomials as basis functions that are completely discontinuous across element boundaries. The DG method will be formulated for the elastodynamics problems under the multiscale setting.

Stable and convergent DG methods have been designed for linear and nonlinear partial differential equations (PDEs) including hyperbolic conservation laws [14, 16], convection-diffusion equations [15], elliptic equations [3], and dispersion wave equations [49]. Comparing with traditional Galerkin methodology (e.g. [28]), the advantage of the DG methods includes their flexibility in h - p adaptivity and parallel efficiency. We refer to, e.g. [17] for a review of the DG methods. For our purpose, the DG methods provide their advantage in the ability of resolving sharp wave fronts, and they can accommodate a locally curl-free function space for the deformation gradient to provide a coherent displacement field, following the local structure preserving DG methodology in [12, 35]. We remark that, in the recent years, there have been many contributions in developing DG methods for solving PDEs in solid mechanics. In most cases, attention has been restricted to linear elasticity problems. For example, Rivière et al. [41] formulated and analyzed a DG method for linear elasticity based on a generalization of the nonsymmetric interior penalty DG method for the diffusion equation. Käser et al. [30, 22] proposed a DG method in space that uses the arbitrary high-order derivatives (ADER) approach for the time integration to solve the linear elastic wave equation in heterogeneous media on unstructured meshes for both two- and three-dimension. Huang and Costanzo [27, 19] proposed a space-time DG formulation for linear-elasticity where stress discontinuities were considered through jumps in the material properties, see also [31]. Abedi et al. [1] proposed a space-time DG method for linearized elastodynamics that delivered exact balance of linear and angular momentum over every space-time element.

The main purpose of this paper is to present a multiscale methodology for transient elastodynamics problems based on the DG methods as a macro solver. We will discuss how the DG methods can be used to capture large scale elastic field, and how the molecular dynamics can be used at the atomic

scale and coupled to the macroscale DG solver to provide accurate constitutive data.

2 Macroscopic and microscopic models

Our computation involves models at both macroscopic and microscopic scales: elastodynamics on the macroscopic scale, describing the evolution of the elastic field, and molecular dynamics at the atomic scale, providing the constitutive data based on detailed atomic interactions. In this section, we briefly present the equations underlying these models.

On the continuum scale, the governing equations for the elastodynamics are a set of PDEs. To begin with, we fix a reference coordinate, denoted by \mathbf{x} , and after deformation, the point will be displaced to a new position, $\mathbf{x} + \mathbf{u}(\mathbf{x}, t)$, with \mathbf{u} being the displacement. Let $\varepsilon = \nabla \mathbf{u}$ be the corresponding deformation gradient. Then the continuum equations take the form:

$$\begin{cases} \frac{\partial}{\partial t} \varepsilon - \nabla \mathbf{v} & = 0, \\ \rho_0 \frac{\partial}{\partial t} \mathbf{v} - \nabla \cdot P & = 0, \\ \rho_0 \frac{\partial}{\partial t} e + \nabla \cdot \mathbf{j} & = 0. \end{cases} \quad (2.1)$$

Here \mathbf{v} and e are the velocity and specific energy per particle respectively, ρ_0 is the initial density, P is the first Piola-Kirchhoff stress tensor and \mathbf{j} is the energy flux. The first equation in (2.1) describes the time evolution of the deformation; the second and third equations are the conservation of momentum and energy respectively. In continuum mechanics, for instance [33], these equations are supplemented by the empirical constitutive relations for stress and energy fluxes. The purpose of the present paper is to develop multiscale strategies that bypass these empirical constitutive laws when their accuracy is in doubt.

At the atomic scale, the motion of the atoms constituting the solids is given by molecular dynamics,

$$\begin{cases} \dot{\mathbf{q}}_i & = \mathbf{p}_i/m_i, \\ \dot{\mathbf{p}}_i & = -\nabla_{\mathbf{q}_i} V, \end{cases} \quad (2.2)$$

where m_i denotes the mass of the i th atom, \mathbf{q}_i and \mathbf{p}_i are the generalized coordinate and momentum for the i th atom, and $V(\mathbf{q}_1, \mathbf{q}_2, \dots, \mathbf{q}_N)$ is the interatomic potential that models the interaction among the atoms. In this

paper, we will only consider pair potential. Namely,

$$V = \frac{1}{2} \sum_{i \neq j} \phi(r_{ij}), \quad r_{ij} = |\mathbf{r}_{ij}|, \quad \mathbf{r}_{ij} = \mathbf{q}_i - \mathbf{q}_j.$$

Many-body potential models, such as the embedded atom model (EAM) [21] and Tersoff-Brenner model [46], can be dealt with similarly. The system (2.2) is a Hamiltonian system with the Hamiltonian

$$H(\mathbf{q}, \mathbf{p}) = \sum_i \frac{\mathbf{p}_i^2}{2m_i} + V(\mathbf{q}), \quad \mathbf{q} = (\mathbf{q}_1, \mathbf{q}_2, \dots, \mathbf{q}_N), \quad \mathbf{p} = (\mathbf{p}_1, \mathbf{p}_2, \dots, \mathbf{p}_N). \quad (2.3)$$

The basic assumption in our current method is the scale separation. Namely the relaxation time for the microscopic processes is much shorter than the typical time scale of the continuum. In this case, it suffices to consider the local equilibrium distribution of the atomistic system. In the case of zero temperature, this is equivalent to the Cauchy-Born hypothesis, which suggests that the atomic displacement follow the macroscopic deformation. As a result, the strain energy density and elastic stress can be computed from the atomistic models. At finite temperature, one has to take into account the thermal fluctuation and compute elastic properties based on statistical ensembles. In this paper, we consider two statistical equilibrium: the micro-canonical distribution,

$$\rho_1(\mathbf{q}, \mathbf{p}) = \frac{1}{Z} \delta(E - H), \quad (2.4)$$

where the volume and the energy of the system are prescribed, and the canonical distribution,

$$\rho_2(\mathbf{q}, \mathbf{p}) = \frac{1}{Z} e^{-\beta H}, \quad \beta = (k_B T)^{-1} \quad (2.5)$$

where the volume and the temperature are given. The constant Z , which is the partition function, normalizes the probability density. Although these statistical ensembles are in principle equivalent in the infinite volume limit, one might have more practical convenience than the other. Once the equilibrium distribution is available, physical observables can be computed via statistical averaging. More specifically, let w be any observable with a microscopic expression $w(\mathbf{q}, \mathbf{p})$. Then

$$\langle w \rangle = \int w(\mathbf{q}, \mathbf{p}) \rho(\mathbf{q}, \mathbf{p}) d\mathbf{q} d\mathbf{p}. \quad (2.6)$$

In a molecular dynamics simulation, we can replace the ensemble average by a time average,

$$\langle w \rangle = \lim_{T \rightarrow \infty} \frac{1}{T} \int_0^T w(\mathbf{q}(t), \mathbf{p}(t)) dt, \quad (2.7)$$

provided that the system is ergodic.

The remaining step in the atomic/continuum coupling is to define the corresponding macroscopic quantities at the atomic scale. Since the continuum equations (2.1) are expressed in the Lagrangian coordinate, we first define the reference coordinate for the atoms as the equilibrium positions, denoted by Q_i . Next we will mainly focus on the calculation of the stress tensor. The first approach to define stress from atomic scale is from thermodynamics [7]. For the atomistic system, the free energy is defined as,

$$\mathcal{F} = -k_B T \ln \int e^{-\beta H} d\mathbf{q} d\mathbf{p}.$$

Implicit in the integral is the dependence on the deformation gradient ε , which changes the volume and shape of the entire system. Here periodic boundary condition is assumed. From the second law of thermodynamics, we have,

$$\frac{1}{\Omega} \frac{\partial \mathcal{F}}{\partial \varepsilon} = P,$$

fixing the temperature. Here Ω is the volume of the system in the reference coordinate. This calculation yields,

$$P = \frac{1}{\Omega} \sum_{i < j} \phi'(r_{ij}) \frac{\mathbf{r}_{ij} \otimes Q_{ij}}{r_{ij}^2}, \quad Q_{ij} = Q_i - Q_j. \quad (2.8)$$

A more natural approach to derive the microscopic expressions is based on conservation laws at the atomic scale [29]. More specifically, we define the local momentum and energy

$$\begin{cases} \tilde{\mathbf{q}}(\mathbf{x}, t) &= \sum_i \mathbf{q}_i(t) \delta(\mathbf{x} - Q_i), \\ \tilde{e}(\mathbf{x}, t) &= \frac{1}{2} \sum_i \left[\frac{\mathbf{p}_i^2}{m_i} + \sum_{j \neq i} \phi(\mathbf{q}_i(t) - \mathbf{q}_j(t)) \right] \delta(\mathbf{x} - Q_i). \end{cases} \quad (2.9)$$

As a result, the total momentum and energy in a control volume can be easily computed. Furthermore, one can derive conservation laws for the local

momentum and energy,

$$\begin{cases} \frac{\partial \tilde{\mathbf{q}}}{\partial t} - \nabla \cdot \tilde{\mathbf{P}} = 0, \\ \rho_0 \frac{\partial \tilde{\epsilon}}{\partial t} + \nabla \cdot \tilde{\mathbf{j}} = 0. \end{cases} \quad (2.10)$$

where,

$$\begin{cases} \tilde{P}(\mathbf{x}, t) = \frac{1}{2} \sum_{i \neq j} \phi'(\mathbf{q}_i - \mathbf{q}_j) \otimes (Q_i - Q_j) \\ \quad \times \int_0^1 \delta(\mathbf{x} - (\mathbf{Q}_j + \lambda(Q_i - Q_j))) d\lambda, \\ \tilde{\mathbf{j}}(\mathbf{x}, t) = \frac{1}{4} \sum_{i \neq j} (\mathbf{p}_i/m_i + \mathbf{p}_j/m_j) \cdot \phi'(\mathbf{q}_i - \mathbf{q}_j) \otimes (Q_i - Q_j) \\ \quad \times \int_0^1 \delta(\mathbf{x} - (\mathbf{Q}_j + \lambda(Q_i - Q_j))) d\lambda. \end{cases} \quad (2.11)$$

Averaging (2.11) in space, one also arrives at (2.8).

Equations (2.1) and (2.10) have been the starting point of HMM: the continuum and atomistic models can be coupled at the level of conservation laws. Such observation is also reminiscent of the concept of local equilibrium in the kinetic theory for gas dynamics, where the Maxwellian distribution can be used to provide the equation of state, and therefore close the continuum equations.

3 Numerical methodology

3.1 Macroscale solver: the DG method

In this paper, the discontinuous Galerkin (DG) and the local discontinuous Galerkin (LDG) methods are used as our macroscale solver. We will briefly review the DG method for solving hyperbolic problems and the LDG method for solving parabolic problems. For more details, we refer the reader to the series of papers of Cockburn, Shu and their coworkers [14, 13, 11, 16], the lecture notes [10] and the review paper [17].

To briefly illustrate the ideas, consider a one-dimensional conservation law on a given interval $I = [a, b]$:

$$u_t + f(u)_x = 0.$$

We divide interval I into N cells as follows,

$$a = x_{\frac{1}{2}} < x_{\frac{3}{2}} < \dots < x_{N+\frac{1}{2}} = b. \quad (3.1)$$

We denote

$$I_i = (x_{i-\frac{1}{2}}, x_{i+\frac{1}{2}}), \quad x_i = \frac{1}{2}(x_{i-\frac{1}{2}} + x_{i+\frac{1}{2}}) \quad (3.2)$$

and

$$\Delta x_i = x_{i+\frac{1}{2}} - x_{i-\frac{1}{2}}, \quad h = \max_i \Delta x_i. \quad (3.3)$$

Next we define the approximation space as

$$V_h^k = \{v_h : (v_h)|_{I_i} \in P^k(I_i), i = 1, \dots, N\}. \quad (3.4)$$

Here $P^k(I_i)$ denotes the set of all polynomials of degree at most k in the interval I_i . For simplicity, we will use the notations u and v instead of u_h , v_h to denote the numerical solutions whenever they do not cause confusion. We can choose a basis of $P^k(I_i)$ as, for example, $\{1, \xi_i, \dots, \xi_i^k\}$, where the monomials $\xi = \frac{x-x_i}{\Delta x_i}$. For a function $v \in V^k$, we use $v_{i+\frac{1}{2}}^-$ and $v_{i+\frac{1}{2}}^+$ to refer to the left and right limit of v at $x_{i+\frac{1}{2}}$, respectively, at the interface where v is discontinuous.

The formulation of the DG method is as follows: find $u(\cdot, t) \in V_h^k$ such that for any test functions $v \in V_h^k$,

$$\int_{I_i} u_i v dx - \int_{I_i} f(u) v_x dx + \widehat{f(u)}_{i+\frac{1}{2}} v_{i+\frac{1}{2}}^- - \widehat{f(u)}_{i-\frac{1}{2}} v_{i-\frac{1}{2}}^+ = 0. \quad (3.5)$$

The single-valued flux $\widehat{f}_{i+\frac{1}{2}}$ should be taken as a monotone flux depending on both $u_{i+\frac{1}{2}}^-$ and $u_{i+\frac{1}{2}}^+$ (exact or approximate Riemann solvers in the system case); see, for example, [34]. We will choose the numerical fluxes to be the Lax-Friedrichs flux

$$\widehat{f}_{i+\frac{1}{2}} = \frac{1}{2}(f_{i+\frac{1}{2}}^- + f_{i+\frac{1}{2}}^+ - \alpha(u_{i+\frac{1}{2}}^+ + u_{i+\frac{1}{2}}^-)), \quad (3.6)$$

where $\alpha = \max |f'(u)|$.

Time discretization is done by the nonlinearly stable high order TVD Runge-Kutta methods developed in [43]. In particular, the second- and third-order TVD Runge-Kutta methods are used to match the corresponding spatial accuracy in our paper. For solving the method of the lines ODE

$$u_t = L(u), \quad (3.7)$$

where $L(u)$ can be any spatial discretization of u , the second-order TVD Runge-Kutta method is given by

$$\begin{aligned} u^{(1)} &= u^n + \Delta t L(u^n) \\ u^{n+1} &= \frac{1}{2}u^n + \frac{1}{2}u^{(1)} + \frac{1}{2}\Delta t L(u^{(1)}), \end{aligned} \quad (3.8)$$

and the third-order TVD Runge-Kutta method is given by

$$\begin{aligned} u^{(1)} &= u^n + \Delta t L(u^n) \\ u^{(2)} &= \frac{3}{4}u^n + \frac{1}{4}u^{(1)} + \frac{1}{4}\Delta t L(u^{(1)}) \\ u^{n+1} &= \frac{1}{3}u^n + \frac{2}{3}u^{(2)} + \frac{2}{3}\Delta t L(u^{(2)}). \end{aligned} \quad (3.9)$$

Since the DG method may have oscillations when the solutions contain discontinuities, nonlinear total variation bounded (TVB) limiters are often used. The limiter we use in this paper is briefly described below. For more details we refer the readers to Shu [42] and Cockburn et al. [13, 16]. Denote

$$u_{i+\frac{1}{2}}^- = \bar{u}_i + \tilde{u}_i, \quad u_{i-\frac{1}{2}}^+ = \bar{u}_i - \tilde{u}_i, \quad (3.10)$$

where \bar{u}_i is the cell average. \tilde{u}_i and \tilde{u}_i are modified by

$$\tilde{u}_i^{(mod)} = m(\tilde{u}_i, \bar{u}_{i+1} - \bar{u}_i, \bar{u}_i - \bar{u}_{i-1}), \quad \tilde{u}_i^{(mod)} = m(\tilde{u}_i, \bar{u}_{i+1} - \bar{u}_i, \bar{u}_i - \bar{u}_{i-1}), \quad (3.11)$$

where the minmod function m is given by

$$m(a_1, a_2, \dots, a_n) = \begin{cases} s \cdot \min_{1 \leq j \leq n} |a_j| & \text{if } \text{sign}(a_1) = \dots = \text{sign}(a_n) = s, \\ 0 & \text{otherwise,} \end{cases} \quad (3.12)$$

or by the TVB modified minmod function [42]

$$\tilde{m}(a_1, a_2, \dots, a_n) = \begin{cases} a_1 & \text{if } |a_1| \leq Mh^2 \\ m(a_1, a_2, \dots, a_n) & \text{otherwise,} \end{cases} \quad (3.13)$$

where $M > 0$ is a constant. The choice of M depends on the solutions of the problem. For the scalar case, it is possible to estimate M (M is related to the magnitude of the second derivatives of the solution at smooth extrema); however, it is more difficult for systems. In our paper, we apply the limiter to

every component of the system with a suitable M (which may not necessarily be the optimal M).

In the case where diffusion terms are present, e.g. the convection-diffusion problems

$$u_t + f(u)_x = (a(u, x)u_x)_x, \quad (3.14)$$

where $a(x) \geq 0$, the idea of the LDG method [15] is to rewrite (3.14) into a first order system

$$u_t - (a(u, x)w)_x = 0, \quad w - u_x = 0. \quad (3.15)$$

We can then formally use the same DG method for the convection equation to solve (3.15), resulting in the following scheme: find $u(., t), w(., t) \in V_h^k$ such that

$$\int_{I_i} u_t v dx + \int_{I_i} a(u, x) w v_x dx - \widehat{a} w_{i+\frac{1}{2}}^- v_{i+\frac{1}{2}}^- + \widehat{a} w_{i-\frac{1}{2}}^+ v_{i-\frac{1}{2}}^+ = 0 \quad (3.16)$$

$$\int_{I_i} w z dx + \int_{I_i} u z_x dx - \widehat{u}_{i+\frac{1}{2}} z_{i+\frac{1}{2}}^- + \widehat{u}_{i-\frac{1}{2}} z_{i-\frac{1}{2}}^+ = 0 \quad (3.17)$$

for all test functions $v, z \in V_h^k$. In [15], criteria are given for these fluxes to guarantee stability, convergence, and a suboptimal error estimate of order k in the L_2 norm for piecewise polynomials of degree k . A clever choice of fluxes in an alternating way

$$\widehat{u}_{i+\frac{1}{2}} = u_{i+\frac{1}{2}}^-, \quad \widehat{w}_{i+\frac{1}{2}} = w_{i+\frac{1}{2}}^+ \quad (3.18)$$

or

$$\widehat{u}_{i+\frac{1}{2}} = u_{i+\frac{1}{2}}^+, \quad \widehat{w}_{i+\frac{1}{2}} = w_{i+\frac{1}{2}}^- \quad (3.19)$$

would satisfy these criteria and give a scheme of order $k + 1$.

3.2 Molecular dynamics simulation

In computing the elastic stress from the microscopic model, we prepare the atomistic system as follows. We first arrange the atoms to the equilibrium position, Q_j , and then apply a uniform deformation, $\mathbf{q}_j = (I + A)Q_j$. The major axes of the simulation box are also deformed accordingly. Periodic boundary conditions are applied with respect to the deformed box to maintain the deformation gradient throughout the computation. The initial

velocity for the atoms is sampled from a Gaussian distribution with the variance given by $k_B T$. In order to maintain the system at a given temperature, we use the standard Nosé-Hoover thermostat [40, 26]. To ensure numerical stability, the time step is chosen so that $\delta t \leq 2/\omega_{max}$, where ω_{max} is the largest phonon frequency. During the simulation, the stress is sampled every 20 time steps, and then averaged at the end of the simulation according to (2.7). In addition the Verlet list method is used to speed up the force calculation. These standard techniques can be found in [25].

3.3 The multiscale method

Having described the methodology for solving the atomistic and continuum equations, we are now in a position to describe the multiscale method. The coupling strategy is quite straightforward: we first divide the computational domain into cells over which the macroscale equations (2.1) are discretized. In computing the numerical fluxes, the stress and heat flux are obtained directly from the atomistic model, either from a molecular dynamics simulation, or from a simplified model, also calibrated from atomistic simulations beforehand (see next section). This procedure can be demonstrated from Fig. 3.1. Comparing to the conventional numerical procedure, we have used atomistic model as a supplemental component on each cell to supply the constitutive data.

4 One-dimensional shock propagation

In our first example the system is described at the atomistic level by a Lennard-Jones potential:

$$\phi(r) = 4\varepsilon \left(\left(\frac{\sigma}{r} \right)^{12} - \left(\frac{\sigma}{r} \right)^6 \right). \quad (4.1)$$

All the particles are assumed to have mass m . In the molecular dynamics simulation, the parameters ε and σ are normalized to unit. As a result, all the computational results are expressed in terms of reduced units, represented by m , ε and σ . The atomistic system is two-dimensional and it is constrained to a narrow slab so that the macroscopic dynamics is essentially

one-dimensional. The continuum equations then reduce to

$$\begin{cases} \partial_t \varepsilon_{11} - \partial_x v_1 &= 0, \\ \rho_0 \partial_t v_1 - \partial_x P_{11} &= 0, \\ \rho_0 \partial_t e - \partial_x (P_{11} v_1) &= 0. \end{cases} \quad (4.2)$$

The initial condition for the macroscale quantities is set up as follows: For the $x < 0$ half plane, we impose a uniform deformation gradient $\varepsilon_{11} = -0.01$, and for the other half plane, the deformation gradient is zero. The system starts from zero velocity and the temperature $T = 0.1$ on the left half plane, and $T = 0.3$ on the right half plane. From the continuum viewpoint, this is an example of the Riemann problem.

We apply the multiscale procedure described above to this problem with the DG method as the macroscale solver. The P^1 and P^2 (second and third order based on piecewise linear and quadratic polynomials) DG results are both presented. The numerical results are shown in Fig. 4.1. As a comparison, we also compute the solution with the second-order Lax-Friedrichs type central schemes, described in Nessyahu and Tadmor [39]. At $t > 0$, one observes two shocks separated by a contact discontinuity. We can see that the DG method captures the discontinuities very well. This type of results have also been confirmed by a full atomistic simulation [36].

5 Two-dimensional case

In our next simulation, the atomistic model is a three-dimensional Lennard-Jones solid with the face-centered cubic (FCC) structure. We consider a system in a state of plain strain so that the macro scale behavior is essentially two-dimensional.

5.1 Atomistic-based constitutive models

The energy flux \mathbf{j} in the continuum equations (2.1) can be written as

$$\mathbf{j} = -(\mathbf{v}^T P + \mathbf{q}), \quad (5.1)$$

with \mathbf{q} being the heat flux.

In principle the heat flux can be computed from an atomistic simulation with a consistent temperature gradient [36]. However such simulations

typically take much longer time to relax, making the computation rather expensive. As an alternative, we model the heat flux by the Fourier law,

$$\mathbf{q} = \kappa \nabla T, \quad (5.2)$$

which has been confirmed via numerous numerical studies [8]. The heat conductivity has been precomputed from the atomistic model. In the following computations, we will consider both the case with the heat flux as well as the one without the heat flux.

In the case of small deformation and low temperature, a linear approximation can be made to provide an explicit stress strain relation:

$$P_{ij} = c_{ijkl}\varepsilon_{kl} + \alpha T \delta_{ij} \quad i, j, k, l = 1, 2 \quad (5.3)$$

where c_{ijkl} are elastic parameters. They can be computed directly from the atomistic model [4]. In particular, we have

$$\begin{cases} P_{11} &= C_{11}\varepsilon_{11} + C_{12}\varepsilon_{22} + \alpha T, \\ P_{12} &= C_{44}(\varepsilon_{12} + \varepsilon_{21}), \\ P_{21} &= P_{12}, \\ P_{22} &= C_{11}\varepsilon_{22} + C_{12}\varepsilon_{11} + \alpha T. \end{cases} \quad (5.4)$$

In terms of the reduced units, these parameters have been obtained from the atomistic model,

$$C_{11} = 97.56753, \quad C_{12} = 55.56524, \quad C_{44} = 55.55364,$$

$$\alpha = -9.91139, \quad \kappa = 0.1925353265.$$

It has been calibrated that under the condition that,

$$\|\varepsilon\|_2 < 0.004 \quad \text{and} \quad T < 0.2, \quad (5.5)$$

the error of this linear approximation (5.4) is within one percent. However this model cannot be directly used because in the PDEs the temperature is not a derived quantity and needs to be obtained from the atomistic models. For this purpose we make another approximation for the temperature,

$$\rho_0 e = E(\varepsilon, T) = E_0 + \frac{1}{2} c_{ijkl} \varepsilon_{kl} \varepsilon_{ij} + 3T. \quad (5.6)$$

Here the first term is the cohesive energy of the crystalline, $E_0 = -7.4591$ per atom, the second term is the familiar form of the strain energy for linear elasticity. In the case of low energy, namely,

$$|E - E_0| < 1.2, \quad (5.7)$$

the modeling error for this approximation (5.6) is also within one percent.

The equations (5.4) and (5.6) provide an efficient constitutive model in the regime of small strain and low temperature. It can be shown that with these constitutive equations, the system of PDEs is hyperbolic (see Appendix A). With the heat flux \mathbf{q} present, the system is of parabolic type.

5.2 Implementation of the constitutive models

While the equilibrium molecular dynamics in principle offers the correct constitutive equation, such procedure is typically computationally intensive, making the overall computation rather expensive. On the other hand, the simplified models in Sec. 5.1 are efficient, but the accuracy can only be guaranteed under small deformation and low temperature. Therefore it is computationally feasible to include both these models in the simulation: we use the constitutive relation (5.4) if the criterion (5.5) is met, and (5.6) if the condition (5.7) is satisfied; Otherwise the data are obtained directly from a molecular dynamics simulation. This reminds us to apply the Domain Decomposition Method (DDM) [9]. The main idea of the DDM is to solve the relatively inexpensive macroscopic model in most part of the computational domain, and only solve the micro problems in the sub-domains where the macroscopic model is not valid.

More specifically, our computational domain can be decomposed to four types of sub-domains. These sub-domains are distinguished by whether the conditions (5.5) and/or (5.7) are satisfied. For example, the first type of sub-domains can be the one satisfying both (5.5) and (5.7). In this case, a computationally inexpensive macro model is sufficient, and we no longer need to do MD. The procedure of using the DDM is: at each time step and in each cell, if the energy is low, namely, if the condition (5.7) is satisfied, we will compute the temperature from (5.6) instead of the MD procedure. After the temperature is obtained, we compute the stress and energy flux from the atomistic model via a canonical ensemble. For small deformation and low temperature, i.e. when (5.5) holds, we use (5.4) to bypass the MD procedure.

In practice, we use parallel computing to speed up our program. At the macro computational domain, for each time step, we first need to get the information of temperature. We label the L cells to be those which satisfy the condition (5.7), and the H cells to be those in which this condition is not satisfied. Then we use the macro relation (5.6) to get the temperature in the L cells. This needs only a negligible cost comparing to MD. For the H cells, we do need to use MD with the canonical ensemble (2.5), which are computationally expensive. To efficiently use all the processors, we collect all the H cells and distribute them to available processors evenly. Next, we need to get the information of the stress tensor. The procedure is the same as above, except that now the condition (5.5) and the relation (5.4) are used to distinguish different types of cells. This procedure is repeated for every macro time step.

5.3 Curl-free discontinuous Galerkin method

In the finite volume representation of the elastic field, it is important to ensure the coherent structure at the cell interface. This issue has been recognized on [1]. In fact the macro scale PDEs are equipped with a natural constraint:

$$\nabla \times \varepsilon = 0,$$

which leads to two pairs of curl-free variables, $(\varepsilon_{11}, \varepsilon_{12})$ and $(\varepsilon_{21}, \varepsilon_{22})$. In order to fulfill the constraints, we choose a curl-free basis for our DG method instead of the standard polynomial basis. The original idea of using curl-free basis is from [12], in which the locally divergence-free DG method is designed to solve the Maxwell equations, and from [35], in which the locally curl-free DG method is designed to solve the Hamilton-Jacobi equations.

In the standard RKDG method, we seek the solution in the finite dimensional polynomial space

$$\bar{\mathbf{V}}_h^{7,k} = \{ \mathbf{v} = (v_1, v_2, v_3, v_4, v_5, v_6, v_7) : \mathbf{v}|_K \in \mathbf{P}^{7,k}(K), K \in \mathcal{K} \} \quad (5.8)$$

where K is the element and \mathcal{K} is the collection of the elements, $\mathbf{P}^{7,k}(K) = (P^k(K))^7$, and $P^k(K)$ denotes the space of polynomials in K of degree at most k . Now we are looking for the solution space whose bases satisfy the

curl-free condition, i.e.

$$\begin{aligned}
\mathbf{V}_h^k &= \left\{ \mathbf{v} \in \bar{\mathbf{V}}_h^{7,k} : \frac{\partial v_1}{\partial y} = \frac{\partial v_2}{\partial x}, \frac{\partial v_3}{\partial y} = \frac{\partial v_4}{\partial x} \right\} \\
&= \left\{ \mathbf{v} = (v_1, v_2) \in \mathbf{P}^{2,k}(K) : \frac{\partial v_1}{\partial y} = \frac{\partial v_2}{\partial x} \right\} \\
&\oplus \left\{ \mathbf{v} = (v_3, v_4) \in \mathbf{P}^{2,k}(K) : \frac{\partial v_3}{\partial y} = \frac{\partial v_4}{\partial x} \right\} \\
&\oplus \left\{ \mathbf{v} = (v_5, v_6, v_7) : \mathbf{v} \in \mathbf{P}^{3,k}(K) \right\} \\
&= \mathbf{V}_h^{2,k} \oplus \mathbf{V}_h^{2,k} \oplus \bar{\mathbf{V}}_h^{3,k}
\end{aligned} \tag{5.9}$$

That is, the vectors (v_1, v_2) and (v_3, v_4) are curl-free polynomial vectors. Notice that the dimension of the space $\mathbf{V}_h^{2,k}$ is $(k+1)(k+4)/2$, only about half as the dimension of $\bar{\mathbf{V}}_h^{2,k}$ which is $(k+1)(k+2)$. Thus the total dimension of the curl free space \mathbf{V}_h^k is (k^2+k) less than the stand piecewise polynomial space $\mathbf{V}_h^{7,k}$, and we can save a lot of computational cost by using the curl free space.

It is very easy to obtain the local bases for $\mathbf{V}_h^{2,k}$. We can take the gradient of the standard bases of $(P^{k+1}(K))$, since we know $\nabla \times \nabla f = 0$ for any scalar function f . For example, if K is the rectangle, with the center (x_i, y_j) and width $\Delta x_i, \Delta y_j$, if we denote

$$\xi = \frac{x - x_i}{\Delta x_i}, \quad \eta = \frac{y - y_j}{\Delta y_j},$$

then one set of bases of $\mathbf{V}_h^{2,k}$ would be, when $k = 1$,

$$\begin{pmatrix} 1 \\ 0 \end{pmatrix}, \begin{pmatrix} \xi \\ 0 \end{pmatrix}, \begin{pmatrix} \Delta y_j \eta \\ \Delta x_i \xi \end{pmatrix}, \begin{pmatrix} 0 \\ 1 \end{pmatrix}, \begin{pmatrix} 0 \\ \eta \end{pmatrix}. \tag{5.10}$$

For $k = 2$, we need to add

$$\begin{pmatrix} \xi^2 \\ 0 \end{pmatrix}, \begin{pmatrix} 2\Delta y_j \xi \eta \\ \Delta x_i \xi^2 \end{pmatrix}, \begin{pmatrix} \Delta y_j \eta^2 \\ 2\Delta x_i \xi \eta \end{pmatrix}, \begin{pmatrix} 0 \\ \eta^2 \end{pmatrix}. \tag{5.11}$$

And for $k = 3$, we need to add

$$\begin{pmatrix} \xi^3 \\ 0 \end{pmatrix}, \begin{pmatrix} 3\Delta y_j \xi^2 \eta \\ \Delta x_i \xi^3 \end{pmatrix}, \begin{pmatrix} \Delta y_j \xi \eta^2 \\ \Delta x_i \xi^2 \eta \end{pmatrix}, \begin{pmatrix} \Delta y_j \eta^3 \\ 3\Delta x_i \xi \eta^2 \end{pmatrix}, \begin{pmatrix} 0 \\ \eta^3 \end{pmatrix}. \tag{5.12}$$

5.4 Numerical results

5.4.1 Comparison of RKDG methods using curl-free P^k and standard P^k bases

In the following example, we consider a system under an external force $\mathbf{h}(x, y, t)$. The macroscale equations take the form of:

$$\begin{cases} \frac{\partial}{\partial t} \varepsilon - \nabla \mathbf{v} &= 0, \\ \rho_0 \frac{\partial}{\partial t} \mathbf{v} - \nabla \cdot P &= h_1(x, y, t), \\ \rho_0 \frac{\partial}{\partial t} e - \nabla \cdot (\mathbf{v}^T P) &= h_2(x, y, t). \end{cases} \quad (5.13)$$

We choose the source terms as

$$\begin{aligned} h_1(x, y, t) &= 0.01(\rho_0 - C_{11} - C_{12} - 2C_{44}) \cos(t + x + y), \\ h_2(x, y, t) &= 0.01^2(\rho_0 - C_{11} - C_{12} - 2C_{44}) \sin(2(t + x + y)). \end{aligned}$$

The initial conditions are given by,

$$\begin{cases} \varepsilon_{ij} &= 0.01 \sin(x + y) \\ v_i &= 0.01 \sin(x + y) \\ \rho_0 e &= E_0 + 0.01^2(C_{11} + C_{12} + 2C_{44}) \sin^2(x + y) \end{cases} \quad i, j = 1, 2 \quad (5.14)$$

and with periodic boundary conditions the exact solutions are

$$\begin{cases} \varepsilon_{ij} &= 0.01 \sin(t + x + y) \\ v_i &= 0.01 \sin(t + x + y) \\ \rho_0 e &= E_0 + 0.01^2(C_{11} + C_{12} + 2C_{44}) \sin^2(t + x + y) \end{cases} \quad i, j = 1, 2 \quad (5.15)$$

We use this set of exact solutions to test the accuracy and efficiency of the curl-free DG method comparing to the standard DG method. We list the L^2 errors and orders of accuracy using P^1 and P^2 DG methods in Tables 5.1, 5.2 and 5.3. The solutions are run to $T = 2\pi$. We can observe the optimal $(k + 1)$ -th order of accuracy both for the standard DG method and the curl-free DG method. The magnitudes of the errors for the same mesh are comparable for the two DG methods.

Table 5.1: L^2 error and order of accuracy for the stress strain ε

mesh	standard P^k		local curl-free P^k	
	L^2 error	order	L^2 error	order
P^1				
10×10	2.12E-03	–	2.12E-03	–
20×20	5.28E-04	2.01	5.27E-04	2.00
40×40	1.31E-04	2.00	1.31E-04	2.00
80×80	3.32E-05	1.98	3.32E-05	1.98
160×160	8.35E-06	1.99	8.35E-06	1.99
P^2				
10×10	2.35E-03	–	1.92E-03	–
20×20	3.25E-04	2.86	2.62E-04	2.87
40×40	4.41E-05	2.88	3.39E-05	2.95
80×80	5.71E-06	2.95	4.33E-06	2.97
160×160	6.93E-07	3.04	5.47E-07	2.98

5.4.2 Thermal expansion

In this example, we study the effect of thermal expansion due to the temperature dependence of the stress. Initially the material is at rest with a homogeneous temperature distribution $T = 0.1$. Our computational domain is a square $[-1, 1] \times [-1, 1]$. We then increase the temperature in the middle $[-0.4, 0.4] \times [-0.4, 0.4]$ instantaneously to $T = 0.4$. This results in a thermal expansion that propagates outwards. We solve the macro equations (2.1) by the DG methods described above, and compare the results with those obtained with the two-dimensional central scheme [39].

We present results in the following two cases: one is without the heat flux, the other is with the heat flux. Without the heat flux, the system is hyperbolic. Therefore it will have discontinuities in the solution under discontinuous initial conditions. In the presence of the heat flux, the system is parabolic. Therefore, the solution becomes smooth at $t > 0$ even if the initial condition is discontinuous. We will demonstrate the numerical results for the temperature distribution as well as the velocity field below.

The simplified constitutive model

We first run the simulation using the linear constitutive model (5.4) and

Table 5.2: L^2 error and order of accuracy for the velocity

mesh	standard P^k		local curl-free P^k	
	L^2 error	order	L^2 error	order
P^1				
10×10	2.29E-02	–	2.28E-03	–
20×20	7.88E-03	1.54	7.88E-03	1.53
40×40	1.96E-03	2.01	1.96E-03	2.01
80×80	4.70E-04	2.06	4.69E-04	2.06
160×160	1.14E-04	2.04	1.14E-04	2.04
P^2				
10×10	2.56E-03	–	2.49E-03	–
20×20	3.03E-04	3.08	2.95E-04	3.08
40×40	3.74E-05	3.02	3.68E-05	3.00
80×80	4.65E-06	3.01	4.63E-06	2.99
160×160	5.77E-07	3.01	5.82E-07	2.99

(5.6) everywhere.

Without the heat flux: The results of the temperature distribution at $t = 0.01$ are shown in Fig. 5.1. The macro solver from left to right in Fig. 5.1 is the DG P^1 , DG P^2 and the second-order central scheme, respectively. We can see that the DG scheme captures the shocks much better than the second-order central scheme using the same mesh. We can also see this from the cross section view of the 3D temperature distribution by the DG and the second-order central scheme in Fig. 5.2. Since we have not used any limiter for the results in the left picture of Fig. 5.2, there are some oscillations near the shocks. The application of limiters can eliminate these oscillations, see Fig. 5.2 right. For both figures, the shocks are sharper for the DG method than for the second-order central scheme.

With the heat flux: Adding the heat flux in our model is adding a diffusion term to the right side of PDEs. The LDG methods can easily deal with the diffusion term. The results of the temperature distribution using both DG P^1 and P^2 at $t = 0.01$ with a 80×80 mesh are shown in Fig. 5.3.

The full MD-based constitutive model

Table 5.3: L^2 error and order of accuracy for the energy

mesh	standard P^k		local curl-free P^k	
	L^2 error	order	L^2 error	order
P^1				
10×10	3.38E-02	–	3.38E-02	–
20×20	7.97E-03	2.08	7.98E-03	2.08
40×40	7.42E-04	3.43	7.42E-04	3.43
80×80	1.75E-04	2.08	1.75E-04	2.08
160×160	4.42E-05	1.98	4.42E-05	1.98
P^2				
10×10	1.34E-01	–	1.12E-01	–
20×20	1.78E-02	2.91	1.54E-02	2.87
40×40	2.29E-03	2.96	1.99E-03	2.95
80×80	2.92E-04	2.97	2.54E-04	2.97
160×160	3.68E-05	2.99	3.21E-05	2.98

In this case, we compute the stress from MD in every cell. We first compute the temperature from the atomistic models. After the temperature is obtained, we compute the stress and energy flux from the atomistic model via a canonical ensemble.

Without the heat flux. The results of the temperature distribution at $t = 0.01$ are shown in Fig. 5.4. We compare our DG method again with the second order central scheme. Using four times as many cells for the second-order central scheme as that for the DG P^1 method, we can still see the advantage of the DG method in capturing shocks. A clearer view in Fig. 5.5 shows the cross section of the 3D temperature distribution computed by the DG P^1 and the second-order central scheme. The results of the velocity field at $t = 0.01$ are shown in Fig. 5.6. The direction of the velocity is pointing outward since the temperature is propagating outward.

With the heat flux. The results of the temperature distribution and the velocity field at $t = 0.01$ are shown in Fig. 5.7.

The domain decomposition model

Here we use the DDM procedure, as described in Sec. 5.2.

Without the heat flux: The results of the temperature distribution and the velocity fields using DG P^1 at $t = 0.01$ by the DDM model are shown in Fig. 5.8.

The results by the DDM are almost the same as the one we obtained by the full MD-based model (see Fig. 5.4 left and 5.6 left). This is more clearly seen from the cross section of the 3D temperature distribution by the DDM and the MD (see Fig. 5.11): they overlap almost completely.

The results of the temperature distribution and the velocity fields using the DG P^1 at $t = 0.03$ by the DDM model are shown in Fig. 5.9. As the time evolves, the heating is expanding outwards.

With the heat flux: The results of the temperature distribution and the velocity fields at $t = 0.01$ are shown in Fig. 5.10. Fig. 5.12 shows the results at $t = 0.03$. We can clearly see a thermal expansion propagating outwards.

The domain decomposition method (DDM) saves lots of computational cost. For example, we need 18 hours using 36 processors to evolve 1 time step with 30×30 cells for the MD DG P^1 method, while we only need less than 3 hours to do the same thing for the DDM. Actually, we only need to run the MD for the high temperature region in the middle. Initially, this part is only 16% of the whole domain. As time evolves, the high heat will propagate outwards and the area becomes even smaller.

5.4.3 Wave propagation

As the last example, we simulate elastic wave propagation in a 2-D unbounded medium. The experiment we present is described in [5]. The major difference is: their governing equations are based on linear elastodynamics, but ours are based on the domain decomposition model. We apply perfectly matched layers (PML) as described in [18] to simulate the propagation of waves in this open domain. See Appendix B for a brief description of the PML method.

Our computational domain is $\Omega = [-5, 5] \times [-5, 5]$ in 2-D, occupied by an elastic material, and we suppose that the initial condition (or the source) is supported in $D = [-3.5, 3.5] \times [-3.5, 3.5] \subset \Omega$. We are solving this elastodynamics problem with absorbing layers (PML) with width $\delta = 1.5$ on all four boundaries.

The initial data of the velocity and the stress are taken to be equal to

zero. The material is of constant temperature $T = 0.167$ everywhere, and it is assumed to stay in the same temperature environment. An explosive source located at the point $(x_s, y_s) = (-3.15, 3.15)$ is introduced to the right side of the equations of conservation of velocity,

$$f((x, y), t) = h(t)g(r)\vec{e}_r. \quad (5.16)$$

where $\vec{e}_r = (x - x_s, y - y_s)$, $r = \|\vec{e}_r\|$. The function $h(t)$ is the so-called second-order Ricker signal with central frequency equal to $f_0 = 10Hz$ (see Fig. 5.13 left):

$$h(t) = [2\pi^2(f_0 t - 1)^2 - 1]e^{-\pi^2(f_0 t - 1)^2}, \quad (5.17)$$

and the function $g(r)$ is the Gaussian function defined by (see Fig. 5.13 right)

$$g(r) = \frac{10e^{-7(r/r_0)^2}}{r_0^2}, \quad (5.18)$$

which is concentrated in a small disk of radius $r_0 = 0.3$.

The damping factor we use is as follows:

$$d(x) = \frac{3c}{2\delta^3} \log\left(\frac{1}{R}\right) x^2, \quad (5.19)$$

where $R = 10^{-3}$ is the theoretical reflection coefficient from the terminating reflection boundaries, i.e., the reflection coefficient is about 0.1%. c is an upper bound of the wave velocities, chosen as $c = 1$ here.

We show the snapshots of the velocity module using DG P^1 by the macro model in Fig. 5.14 and by the DDM model in Fig. 5.15. The PML works very well. The wave fronts are not circles because of the anisotropy of the medium. The waves are propagating outwards. At $t = 0.34$ (see Fig. 5.14, 5.15 upper right), some waves disappear on the upper left corner. The lower right waves are moving downwards as the time goes. At $t = 1.0$ (see Fig. 5.14, 5.15 bottom middle), these waves arrive at the lower right corner. And at $t = 1.5$ (see Fig. 5.14, 5.15 bottom right), the amplitude of velocity module is actually already below 5×10^{-4} .

6 Concluding remarks

We have developed a multiscale solver based on the discontinuous Galerkin (DG) method. The ability of the DG method to treat sharp wave front makes

it particularly suitable for this problem. This has been demonstrated by a few test problems. More importantly it allows us to conveniently use atomistic models to provide constitutive data within the computation. The bottleneck of the method has been the atomistic component where MD is performed to calculate the elastic stress. This has been alleviated to some extent in this paper by first obtaining a simplified model in the case of small strain and low energy/temperature. More efficient methods are needed here to completely bypass MD. This is our current work in progress. Finally even though the numerical tests have been performed using rectangular elements, the DG methodology allows the usage of arbitrary unstructured meshes with a full h - p adaptivity capability.

In the current framework, we have assumed that the material is a single perfect crystal. The next step is to model the dynamics of isolated defects, such as dislocation, phase boundary or crack tips. These problems bring up many interesting issues, such as the boundary conditions at the atomistic/continuum interface (e.g. see [37, 38]), adaptive mesh refinement, thermal fluctuations etc. These issues will be addressed in future work.

A Appendix: The hyperbolicity of the constitutive model without the heat flux

When the deformation is small and the temperature is low, we can use the linearized stress strain relation (5.4) and the linearized temperature relation (5.6) to solve for the temperature T , then we will have a closed system of equations. For the case without the heat flux, this system of equations can be written in the form of a system of conservation laws:

$$\mathbf{U}_t + \mathbf{F}_x + \mathbf{G}_y = 0,$$

where

$$\mathbf{U} = \begin{pmatrix} \varepsilon_{11} \\ \varepsilon_{12} \\ \varepsilon_{21} \\ \varepsilon_{22} \\ \rho_0 v_1 \\ \rho_0 v_2 \\ \rho_0 e + \frac{1}{2} \rho_0 (v_1^2 + v_2^2) \end{pmatrix}, \quad \mathbf{F} = \begin{pmatrix} -v_1 \\ 0 \\ -v_2 \\ 0 \\ -P_{11} \\ -P_{21} \\ -v_1 P_{11} - v_2 P_{21} \end{pmatrix}, \quad \mathbf{G} = \begin{pmatrix} 0 \\ -v_1 \\ 0 \\ -v_2 \\ -P_{21} \\ -P_{22} \\ -v_1 P_{21} - v_2 P_{22} \end{pmatrix} \quad (\text{A.1})$$

with the relations (5.4) and (5.6).

It is known that in [20] (p.55), this system (A.1) is hyperbolic on a certain region of the state space if for every (ε, η) lying in that region, the following two conditions hold,

$$\frac{\partial \hat{E}(\varepsilon, \eta)}{\partial \eta} > 0, \quad (\text{A.2})$$

$$\frac{\partial^2 \hat{E}(\varepsilon, \eta)}{\partial \varepsilon_{ij} \partial \varepsilon_{kl}} \nu_j \nu_l \xi_i \xi_k > 0, \quad \text{for all } \nu \text{ and } \xi, \quad (\text{A.3})$$

where η is the entropy and $\hat{E}(\varepsilon, \eta) = E(\varepsilon, T)$. The first condition ensures that the temperature is positive, and the second condition, often referred to as the rank-one convexity condition, implies that the local thermal equilibrium is stable.

First to compute the entropy $\eta = \eta(\varepsilon, T)$, using the Helmholtz free energy ([20] p.41)

$$\psi(\varepsilon, T) = e(\varepsilon, T) - T\eta, \quad (\text{A.4})$$

we obtain

$$P_{ij} = \rho_0 \frac{\partial \psi}{\partial \varepsilon_{ij}} = \frac{\partial E(\varepsilon, T)}{\partial \varepsilon_{ij}} - \rho_0 T \frac{\partial \eta}{\partial \varepsilon_{ij}} = c_{ijkl} \varepsilon_{kl} - \rho_0 T \frac{\partial \eta}{\partial \varepsilon_{ij}}. \quad (\text{A.5})$$

The last equality comes from the expression of $E(\varepsilon, T)$ given by (5.6).

Applying the definition of P in (5.3) to (A.5), we get

$$\rho_0 T \frac{\partial \eta}{\partial \varepsilon_{ij}} = -\alpha T \delta_{ij}. \quad (\text{A.6})$$

Thus

$$\eta = -\frac{\alpha}{\rho_0} (\varepsilon_{11} + \varepsilon_{22}) + \varphi(T). \quad (\text{A.7})$$

To determine the function $\varphi(T)$, we know from (A.4),

$$\eta(\varepsilon, T) = -\frac{\partial \psi}{\partial T} = -\frac{\partial (e - T\eta)}{\partial T} = -\frac{\partial e}{\partial T} + \eta + T \frac{\partial \eta}{\partial T} = -\frac{3}{\rho_0} + \eta + T \frac{\partial \eta}{\partial T}, \quad (\text{A.8})$$

which then reduces to

$$T \frac{\partial \eta}{\partial T} = \frac{3}{\rho_0}. \quad (\text{A.9})$$

Together with (A.7), we finally obtain the entropy for the system (A.1),

$$\eta(\varepsilon, T) = -\frac{\alpha}{\rho_0}(\varepsilon_{11} + \varepsilon_{22}) + \frac{3}{\rho_0} \log T \quad (\text{A.10})$$

up to a constant.

Next, $\hat{T} = \hat{T}(\varepsilon, \eta)$ can be solved by (A.10),

$$\hat{T}(\varepsilon, \eta) = e^{(\rho_0 \eta + \alpha(\varepsilon_{11} + \varepsilon_{22}))/3}. \quad (\text{A.11})$$

Then

$$\hat{E}(\varepsilon, \eta) = E_0 + \frac{1}{2} c_{ijkl} \varepsilon_{kl} \varepsilon_{ij} + 3e^{(\rho_0 \eta + \alpha(\varepsilon_{11} + \varepsilon_{22}))/3}. \quad (\text{A.12})$$

For the first condition given by (A.2),

$$\frac{\partial \hat{E}(\varepsilon, \eta)}{\partial \eta} = \rho_0 e^{(\rho_0 \eta + \alpha(\varepsilon_{11} + \varepsilon_{22}))/3} > 0. \quad (\text{A.13})$$

The second condition (A.3), called the Legendre-Hadamard condition, means that \hat{E} is rank-one convex in ε . It is equivalent to the condition that the matrix $\left(\frac{\partial^2 \hat{E}(\varepsilon, \eta)}{\partial \varepsilon_{ij} \partial \varepsilon_{kl}} \right)_{4 \times 4}$ is positive definite.

It is easy to check that the matrix

$$\left(\frac{\partial^2 \hat{E}(\varepsilon, \eta)}{\partial \varepsilon_{ij} \partial \varepsilon_{kl}} \right)_{4 \times 4} = \begin{pmatrix} C_{11} + \frac{1}{3} \alpha^2 e^{(\rho_0 \eta + \alpha(\varepsilon_{11} + \varepsilon_{22}))/3} & 0 & 0 & C_{12} + \frac{1}{3} \alpha^2 e^{(\rho_0 \eta + \alpha(\varepsilon_{11} + \varepsilon_{22}))/3} \\ 0 & C_{44} & C_{44} & 0 \\ 0 & C_{44} & C_{44} & 0 \\ C_{12} + \frac{1}{3} \alpha^2 e^{(\rho_0 \eta + \alpha(\varepsilon_{11} + \varepsilon_{22}))/3} & 0 & 0 & C_{11} + \frac{1}{3} \alpha^2 e^{(\rho_0 \eta + \alpha(\varepsilon_{11} + \varepsilon_{22}))/3} \end{pmatrix} \quad (\text{A.14})$$

is positive definite.

Therefore, the system (A.1) is hyperbolic.

B Appendix: PML methods

The idea of the PML is to surround the computational domain with an absorbing layer (the PML region) such that the coupled system possesses the property of generating no reflection at the interface between the free medium and the artificial absorbing medium. The principle ideas of PML has been

first introduced by Bérenger [6]. In [5], the authors have shown that it is possible to write in a systematic way of designing a PML model for a general first-order hyperbolic system. In this section, we will briefly describe the general construction.

Consider a general two dimensional first-order hyperbolic system

$$\begin{aligned} U_t + AU_x + BU_y &= 0, \\ U(t=0) &= U_0, \end{aligned} \tag{B.1}$$

where U is a m -vector, A and B are $m \times m$ matrices. To simplify the presentation, we assume our physical domain is in the left half plane i.e. $[x_1 < 0, x_2 = 0] \times [y_1, y_2]$. The initial condition U_0 is zero on the right half plane. The main idea of the PML model is to couple the equation in the left half-space with an equation in the right half space such that there is no reflection at the interface $y = 0$.

The construction of PML in the x -direction is to split $U = U^{(1)} + U^{(2)}$, such that the unknown $U^{(1)}$ is only associated to the derivatives with respect to x , and $U^{(2)}$ to the derivatives with respect to y . Then we introduce a damping factor $d(x)$ only on $U^{(1)}$. We obtain the system in the following:

$$\begin{aligned} U_t^{(1)} + d(x)U^{(1)} + AU_x &= 0, \\ U_t^{(2)} + BU_y &= 0, \\ U(t=0) &= U_0, \end{aligned} \tag{B.2}$$

where $d(x) = 0$ for $x < 0$, $d(x) \leq 0$, for $x \leq 0$. It is easy to see that U satisfies the same system of equations in the physical domain. The analysis [6] shows that there will be no reflection at the interface between the physical domain and the absorbing layers. Furthermore, the transmitted wave decreases exponentially during its propagation inside the layer.

In our example, the macro equations are a 2D nonlinear system of parabolic equations. We will apply the PML to all the boundaries. So our macro equations can be rewritten in the following form:

$$\begin{aligned} U_t^{(1)} + d(x)U^{(1)} + F_x &= 0, \\ U_t^{(2)} + d(y)U^{(2)} + G_y &= 0, \\ U(t=0) &= U_0, \end{aligned} \tag{B.3}$$

where F and G are in (A.1), $d(x)$ and $d(y)$ are zeros in the physical domain and positive in the absorbing layers.

References

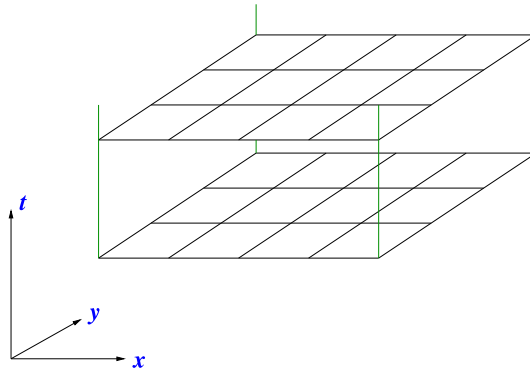
- [1] R. Abedi, B. Petracovici, and R. B. Haber. A space-time discontinuous galerkin method for linearized elastodynamics with element-wise momentum balance. *Comput. Methods. Appl. Mech. Engrg.*, 195(25–28):3247–3273, 2006.
- [2] F. F. Abraham, J. Q. Broughton, N. Bernstein, and E. Kaxiras. Spanning the continuum to quantum length scales in a dynamic simulation of brittle fracture. *Europhys. Lett*, 44(6):783–787, 1998.
- [3] D.N. Arnold, F. Brezzi, B. Cockburn, and L.D. Marini. Unified analysis of discontinuous Galerkin methods for elliptic problems. *SIAM J. Numer. Anal.*, 39(5):1749–1779, 2002.
- [4] N. W. Ashcroft and N. D. Mermin. *Solid State Physics*. Brooks Cole, 1976.
- [5] E. Bécache, S. Fauqueux, and P. Joly. Stability of perfectly matched layers, group velocities and anisotropic waves. *J. Comput. Phys.*, 188(2):399–433, 2003.
- [6] J. P. Bérenger. A perfectly matched layer for the absorption of electromagnetic waves. *J. Comput. Phys.*, 114(2):185–200, 1994.
- [7] D. Brown and S. Neyertz. A general pressure tensor calculation for molecular dynamics simulations. *Mol. Phys.*, 84(3):577–595, 1995.
- [8] H. J. Castejon. Nonequilibrium molecular dynamics calculation of the thermal conductivity of solid materials. *J. Phys. Chem. B*, 107(3):826–828, 2003.
- [9] S. Chen, W. E, Y.-X. Liu, and C.-W. Shu. A discontinuous Galerkin implementation of a domain decomposition method for kinetic-hydrodynamic coupling multiscale problems in gas dynamics and device simulations. *J. Comput. Phys.*, 225(2):1314–1330, 2007.
- [10] B. Cockburn. Discontinuous Galerkin methods for convection-dominated problems. In *High-Order Methods for Computational Physics, Lect. Notes Comput. Sci. Eng. 9*, T. J. Barth and H. Deconinck, eds., pages 69–224. Springer, Berlin, 1999.

- [11] B. Cockburn, S. Hou, and C.-W. Shu. The Runge-Kutta local projection discontinuous Galerkin finite element method for conservation laws IV: The multidimensional case. *Math. Comp.*, 54(190):545–581, 1990.
- [12] B. Cockburn, F. Li, and C.-W. Shu. Locally divergence-free discontinuous Galerkin methods for the Maxwell equations. *J. Comput. Phys.*, 194(2):588–610, 2004.
- [13] B. Cockburn, S.-Y. Lin, and C.-W. Shu. TVB Runge-Kutta local projection discontinuous Galerkin finite element method for conservation laws III: One dimensional systems. *J. Comput. Phys.*, 84(1):90–113, 1989.
- [14] B. Cockburn and C.-W. Shu. TVB Runge-Kutta local projection discontinuous Galerkin finite element method for conservation laws II: General framework. *Math. Comp.*, 52(186):411–435, 1989.
- [15] B. Cockburn and C.-W. Shu. The local discontinuous Galerkin method for time-dependent convection-diffusion systems. *SIAM J. Numer. Anal.*, 35(6):2440–2463, 1998.
- [16] B. Cockburn and C.-W. Shu. TVB Runge-Kutta local projection discontinuous Galerkin finite element method for conservation laws V: multidimensional systems. *J. Comput. Phys.*, 141(2):199–224, 1998.
- [17] B. Cockburn and C.-W. Shu. Runge-Kutta discontinuous Galerkin methods for convection-dominated problems. *J. Sci. Comput.*, 16(3):173–261, 2001.
- [18] F. Collino and C. Tsogka. Application of the PML absorbing layer model to the linear elastodynamic problem in anisotropic heterogeneous media. *Geophysics*, 66(1):294–307, 2001.
- [19] F. Costanzo and H. Huang. Proof of unconditional stability for a single-field discontinuous Galerkin finite element formulation for linear elastodynamics. *Comput. Methods. Appl. Mech. Engrg.*, 194(18–20):2059–2076, 2005.
- [20] C. M. Dafermos. *Hyperbolic Conservation Laws in Continuum Physics*. Springer, second edition, 2005.

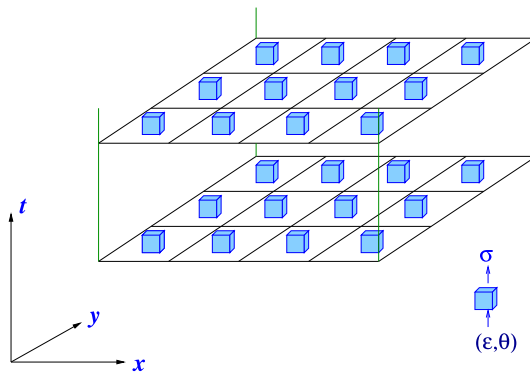
- [21] M. S. Daw and M. I. Baskes. Embedded-atom method: derivation and application to impurities, surfaces, and other defects in metals. *Phys. Rev. B*, 29(12):6443–6453, 1984.
- [22] M. Dumbser and M. Käser. An arbitrary high-order discontinuous Galerkin method for elastic waves on unstructured meshes - II. The three-dimensional isotropic case. *Geophys. J. Int.*, 167(1):319–336, 2006.
- [23] W. E and B. Engquist. The heterogeneous multi-scale methods. *Comm. Math. Sci.*, 1(1):87–132, 2003.
- [24] W. E, B. Engquist, X. Li, W. Ren, and E. Vanden-Eijnden. Heterogeneous multiscale method: A review. *Commun. Comput. Phys.*, 2:367–450, 2007.
- [25] D. Frenkel and B. Smit. *Understanding Molecular Simulation: from Algorithms to Applications*. Academic Press, second edition, 2002.
- [26] W. G. Hoover. Canonical dynamics: Equilibrium phase-space distributions. *Phys. Rev. A*, 31(3):1695–1697, 1985.
- [27] H. Huang and F. Costanzo. On the use of space-time finite elements in the solution of elasto-dynamic problems with strain discontinuities. *Comput. Methods. Appl. Mech. Engrg.*, 191(46):5315–5343, 2002.
- [28] T. J. R. Hughes and G. M. Hulbert. Space-time finite element methods for elastodynamics: formulations and error estimates. *Comput. Methods. Appl. Mech. Engrg.*, 66(3):339–363, 1988.
- [29] J. H. Irving and J. G. Kirkwood. The statistical mechanical theory of transport processes IV. *J. Chem. Phys.*, 18(6):817–829, 1950.
- [30] M. Käser and M. Dumbser. An arbitrary high-order discontinuous Galerkin method for elastic waves on unstructured meshes - I. The two-dimensional isotropic case with external source terms. *Geophys. J. Int.*, 166(2):855–877, 2006.
- [31] D. K. Khalmanova and F. Costanzo. A space-time discontinuous Galerkin finite element method for fully coupled linear thermo-elasto-dynamic problems with strain and heat flux discontinuities. *Comput. Methods. Appl. Mech. Engrg.*, submitted, 2006.

- [32] J. Knap and M. Ortiz. An analysis of the quasicontinuum method. *J. Mech. Phys. Solids*, 49(9):1899–1923, 2001.
- [33] L.D. Landau. *Theory of Elasticity*. Elsevier Science Ltd, 1986.
- [34] R. J. LeVeque. *Numerical Methods for Conservation Laws*. Birkhäuser Basel, 1990.
- [35] F. Li and C.-W. Shu. Reinterpretation and simplified implementation of a discontinuous Galerkin method for Hamilton-Jacobi equations. *App. Math. Lett.*, 18(11):1204–1209, 2005.
- [36] X. Li and W. E. Multiscale modeling for dynamics of solids at finite temperature. *J. Mech. Phys. Solids*, 53(7):1650–1685, 2005.
- [37] X. Li and W. E. Variational boundary conditions for molecular dynamics simulations of solids at low temperature. *Commun. Comput. Phys.*, 1(1):135–175, 2006.
- [38] X. Li and W. E. Variational boundary conditions for molecular dynamics simulations of crystalline solids at finite temperature I: Treatment of the thermal bath. *Phys. Rev. B*, submitted, 2007.
- [39] H. Nessyahu and E. Tadmor. Nonoscillatory central differencing for hyperbolic conservation laws. *J. Comput. Phys.*, 87(2):408–463, 1990.
- [40] S. Nosé. A unified formulation of the constant temperature molecular dynamics method. *J. Chem. Phys.*, 81(1):511–519, 1984.
- [41] B. Rivière, S. Shaw, M. F. Wheeler, and J. R. Whiteman. Discontinuous Galerkin finite element methods for linear elasticity and quasistatic linear viscoelasticity. *Numer. Math.*, 95(2):347–376, 2003.
- [42] C.-W. Shu. TVB uniformly high-order schemes for conservation laws. *Math. Comp.*, 49(179):105–121, 1987.
- [43] C.-W. Shu and S. Osher. Efficient implementation of essentially non-oscillatory shock-capturing schemes. *J. Comput. Phys.*, 77(2):439–471, 1988.
- [44] E. B. Tadmor, M. Ortiz, and R. Phillips. Quasicontinuum analysis of defects in crystals. *Phil. Mag. A*, 73(6):1529–1564, 1996.

- [45] S. Tang, T. Y. Hou, and W. K. Liu. A pseudo-spectral multiscale method: interfacial conditions and coarse grid equations. *J. Comput. Phys.*, 213:57–85, 2006.
- [46] J. Tersoff. New empirical model for the structural properties of silicon. *Phys. Rev. Lett.*, 56(6):632–635, 1986.
- [47] G. J. Wagner and W. K. Liu. Coupling of atomistic and continuum simulations using a bridging scale decomposition. *J. Comput. Phys.*, 190(1):249–274, 2003.
- [48] S. P. Xiao and T. Belytschko. A bridging domain method for coupling continua with molecular dynamics. *Comput. Methods. Appl. Mech. Engrg.*, 193(17–20):1645–1669, 2004.
- [49] J. Yan and C.-W. Shu. A local discontinuous Galerkin method for KdV type equations. *SIAM J. Numer. Anal.*, 40(2):769–791, 2002.



(a) A conventional numerical method.



(b) The heterogeneous multiscale method.

Figure 3.1: Conventional numerical methods and the heterogeneous multiscale methods. In the multiscale method, an additional component, indicated by the small boxes, is applied to compute the elastic stress. Here $\theta = k_B T$.

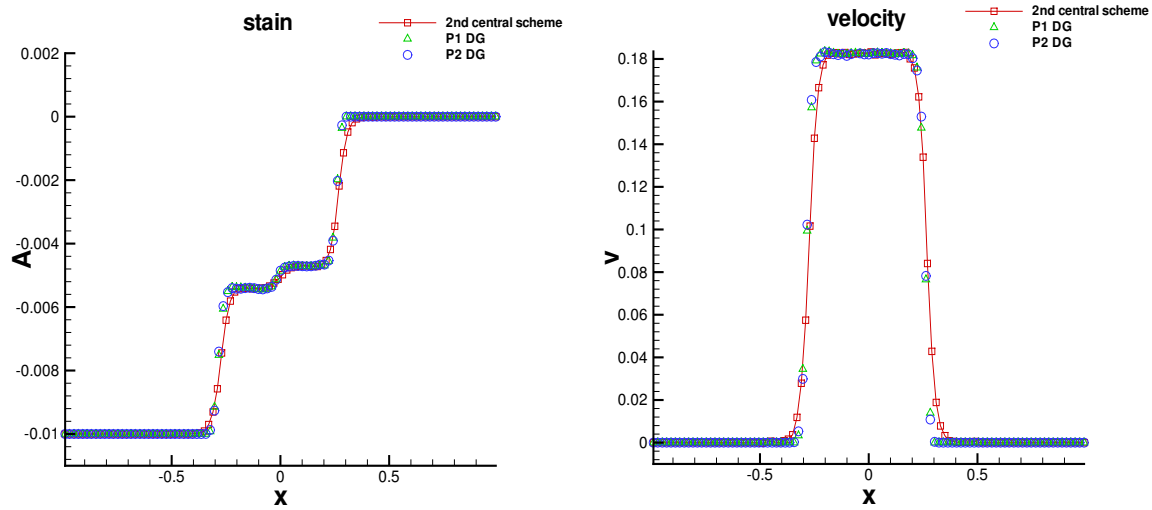


Figure 4.1: Numerical test on 1D shock formation and propagation. 100 macro cells are used. The solutions are displayed at the physical time $T = 0.01$. Solid line with the square symbol: the second-order central scheme; triangle and circle symbols: DG P^1 and P^2 with TVD limiter. Left: strain, right: velocity.

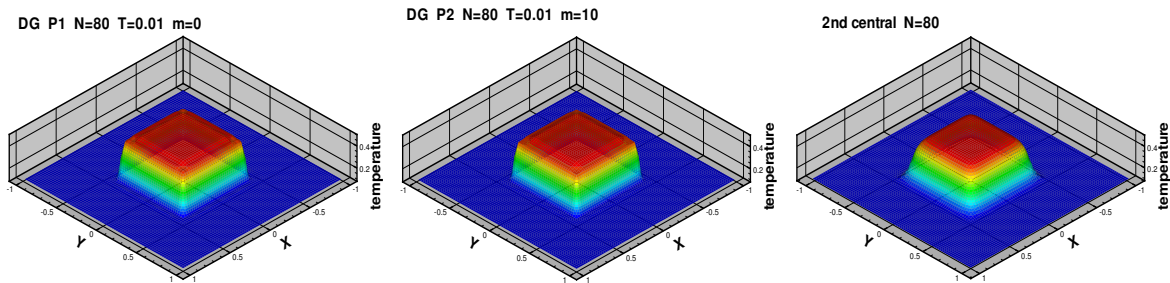


Figure 5.1: Temperature distribution without the heat flux (by the simplified constitutive model) at $t = 0.01$ with 80×80 cells. Left: DG P^1 with the TVD limiter; middle: DG P^2 with the TVB limiter $M = 10$; right: the second-order central scheme.

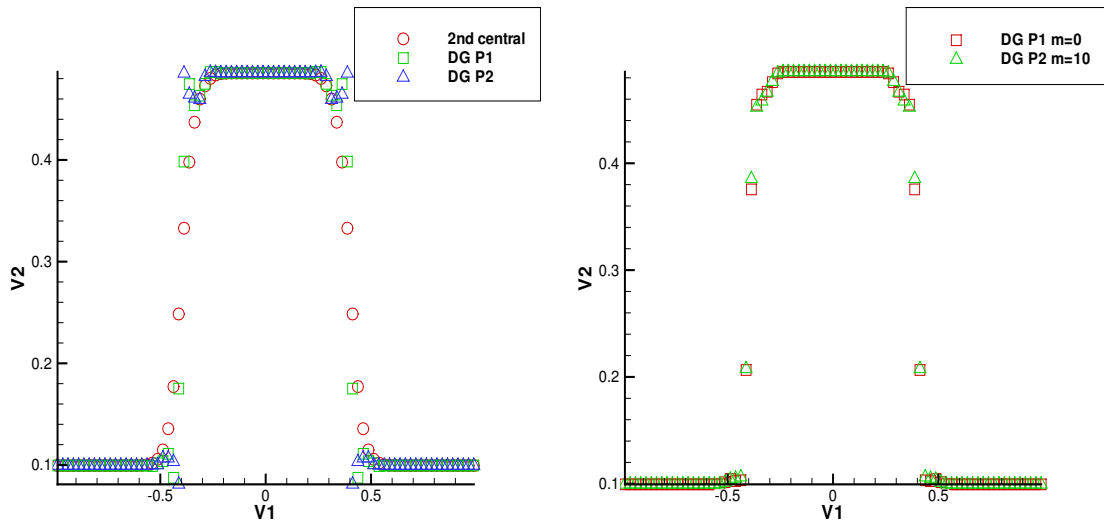


Figure 5.2: Cross section of the 3D temperature distribution without the heat flux (by the simplified constitutive model) at $t = 0.01$ with 80×80 cells. Left: DG P^1 , P^2 without limiters and the second-order central scheme; Right: DG P^1 with the TVD limiter and P^2 with the TVB limiter $M = 10$.

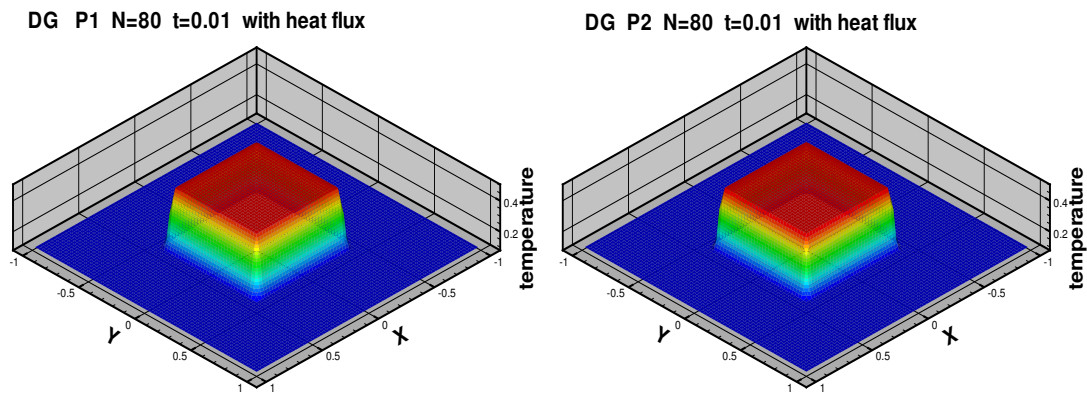


Figure 5.3: Temperature distribution with the heat flux (by the simplified constitutive model) at $t = 0.01$ with 80×80 cells. Left: DG P^1 ; right: DG P^2 .

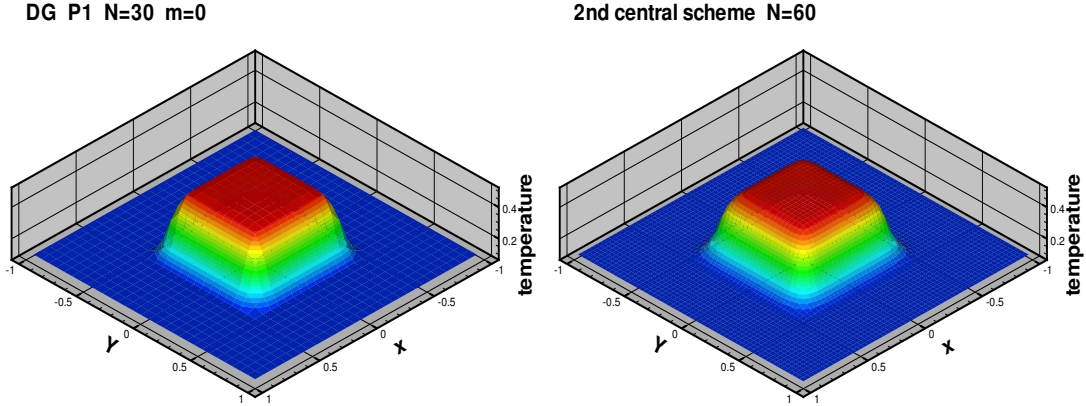


Figure 5.4: Temperature distribution without the heat flux (by the full MD-based model) at $t = 0.01$. Left: DG P^1 with 30×30 cells with the TVD limiter; right: the second-order central scheme with 60×60 cells.

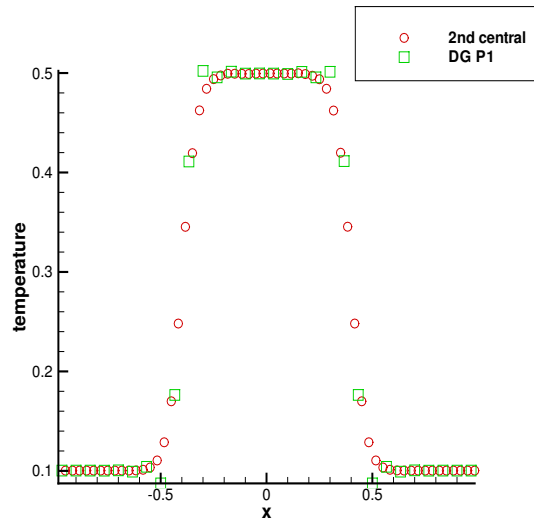


Figure 5.5: Cross section of the 3D temperature distribution without the heat flux (by the full MD-based model) at $t = 0.01$. DG P^1 with 30×30 cells and the second-order central scheme with 60×60 cells.

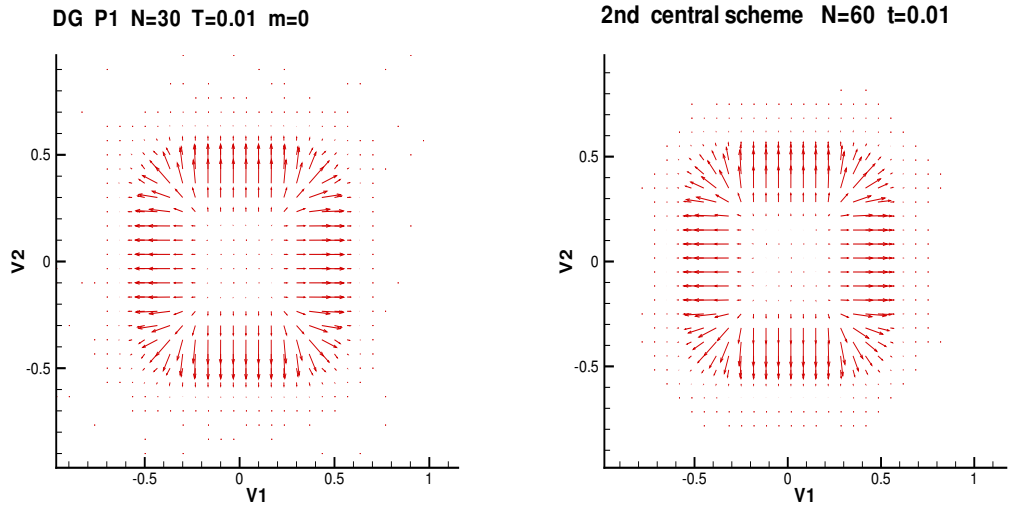


Figure 5.6: The velocity field without the heat flux (by the full MD-based model) at $t = 0.01$. Left: DG P^1 with 30×30 cells with the TVD limiter; right: the second-order central scheme with 60×60 cells.

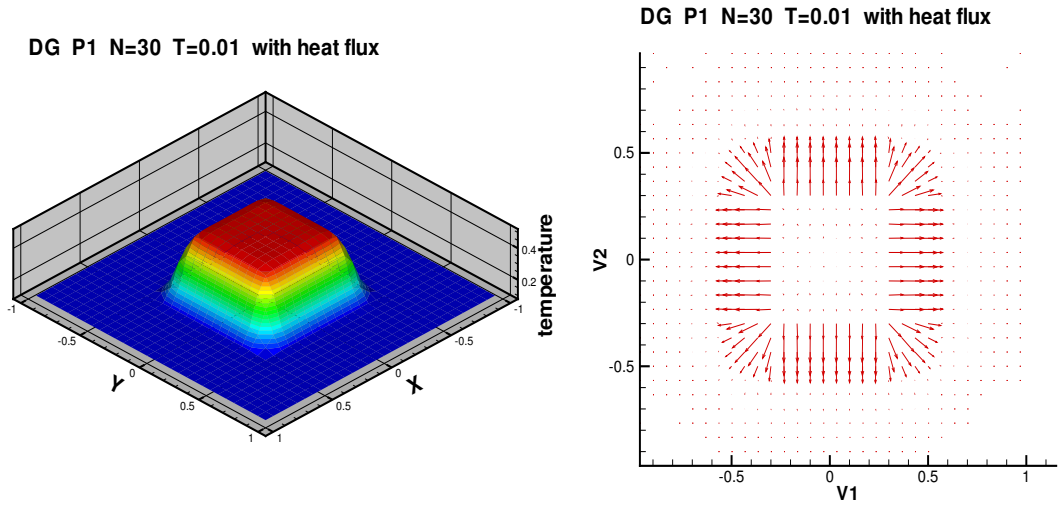


Figure 5.7: With the heat flux at $t = 0.01$. DG P^1 with 30×30 cells (by the full MD-based model). Left: the temperature distribution; right: the velocity field.

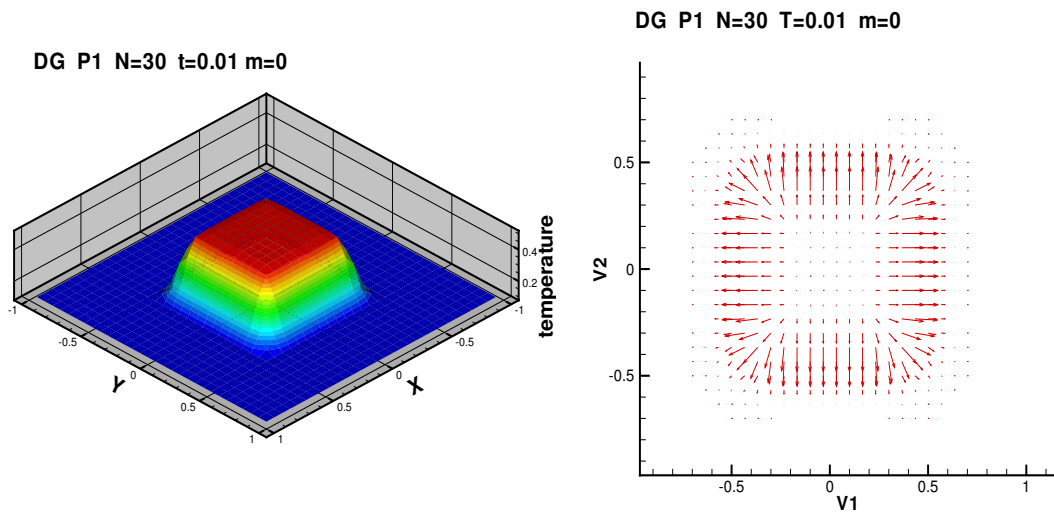


Figure 5.8: Without the heat flux at $t = 0.01$. DG P^1 with 30×30 cells (by the DDM). Left: the temperature distribution; right: the velocity field.

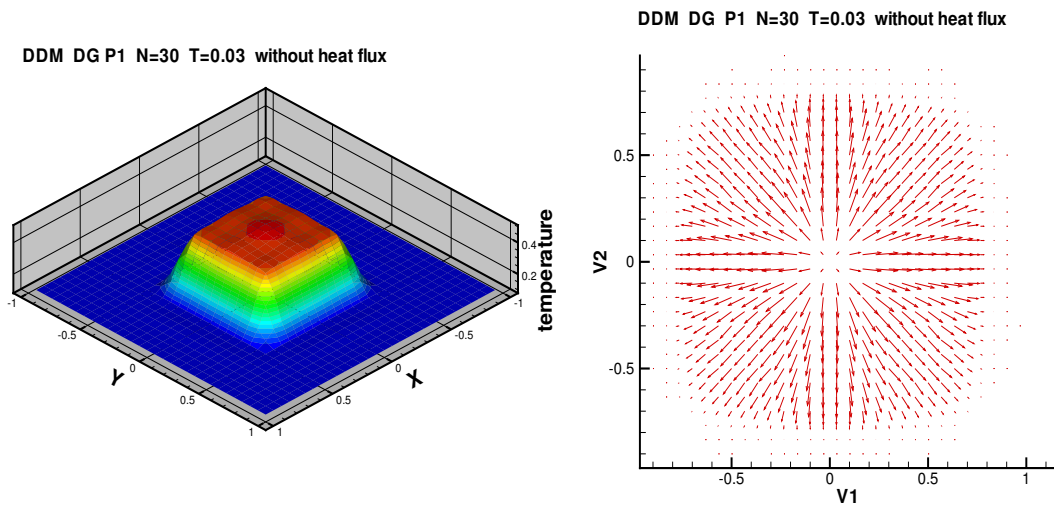


Figure 5.9: Without the heat flux at $t = 0.03$. DG P^1 with 30×30 cells (by the DDM). Left: the temperature distribution; right: the velocity field.

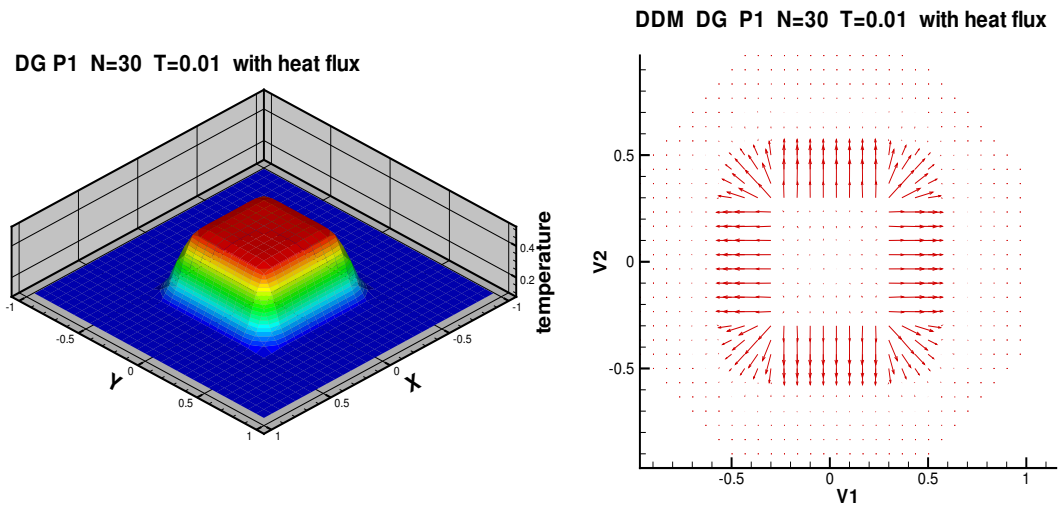


Figure 5.10: With the heat flux at $t = 0.01$. DG P^1 with 30×30 cells (by the DDM). Left: the temperature distribution; right: the velocity field.

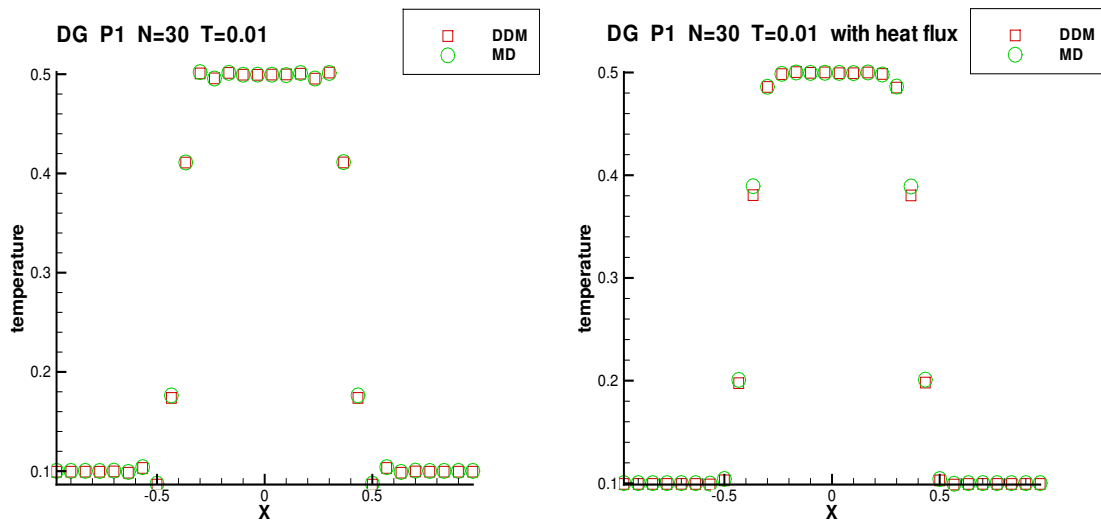


Figure 5.11: Comparison of DDM and full MD-based models: cross section of the 3D temperature distribution at $t = 0.01$. DG P^1 with 30×30 cells. Left: without the heat flux; Right: with the heat flux.

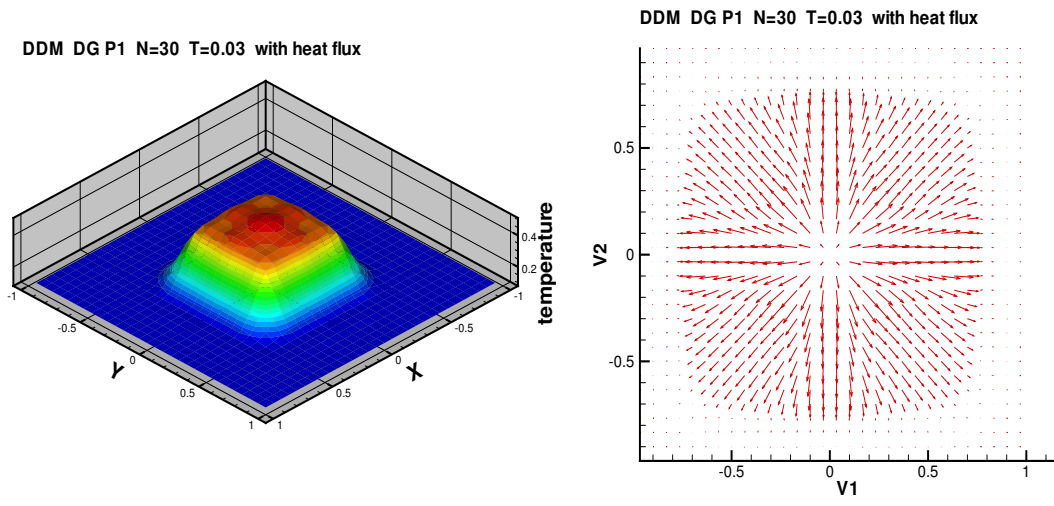


Figure 5.12: With the heat flux at $t = 0.03$. DG P^1 with 30×30 cells (by the DDM). Left: the temperature distribution; right: the velocity field.

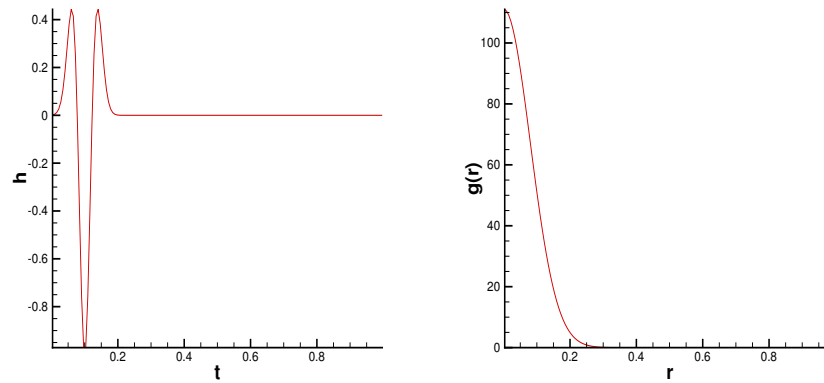


Figure 5.13: Left: the Ricker signal $h(t)$; right: the Gaussian function $g(r)$.

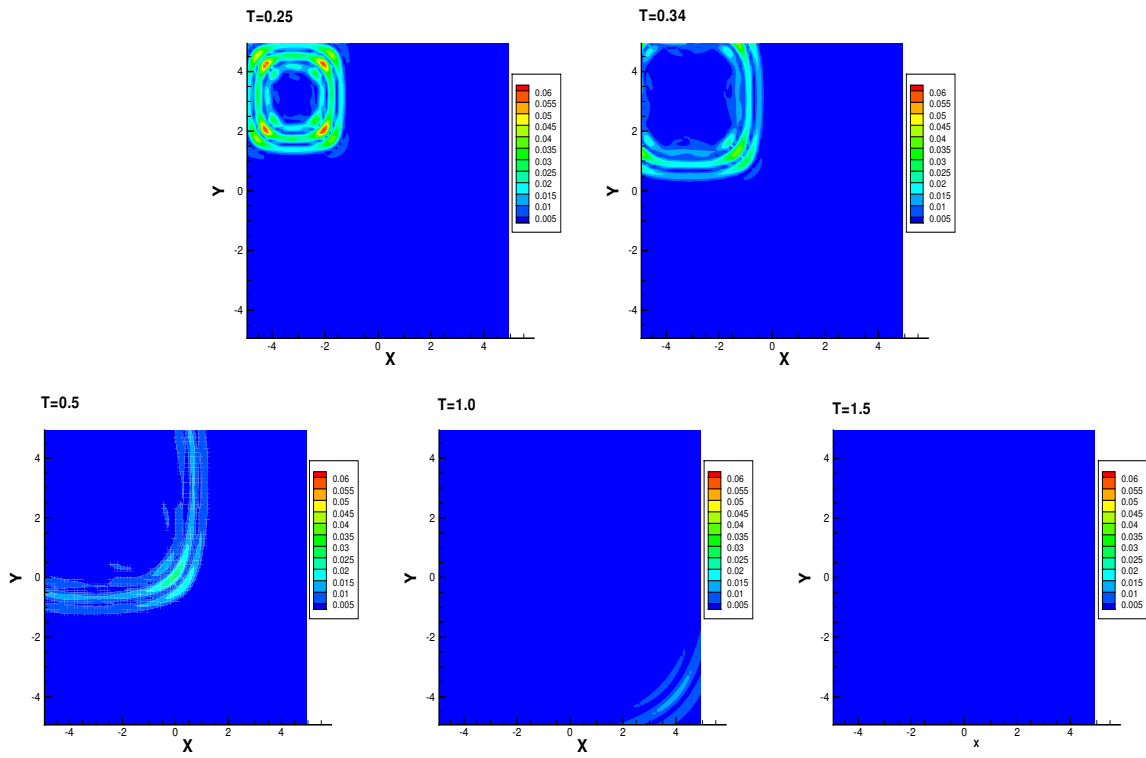


Figure 5.14: Snapshots of the velocity module at different times (by the simplified constitutive model): DG P^1 with 80×80 cells.

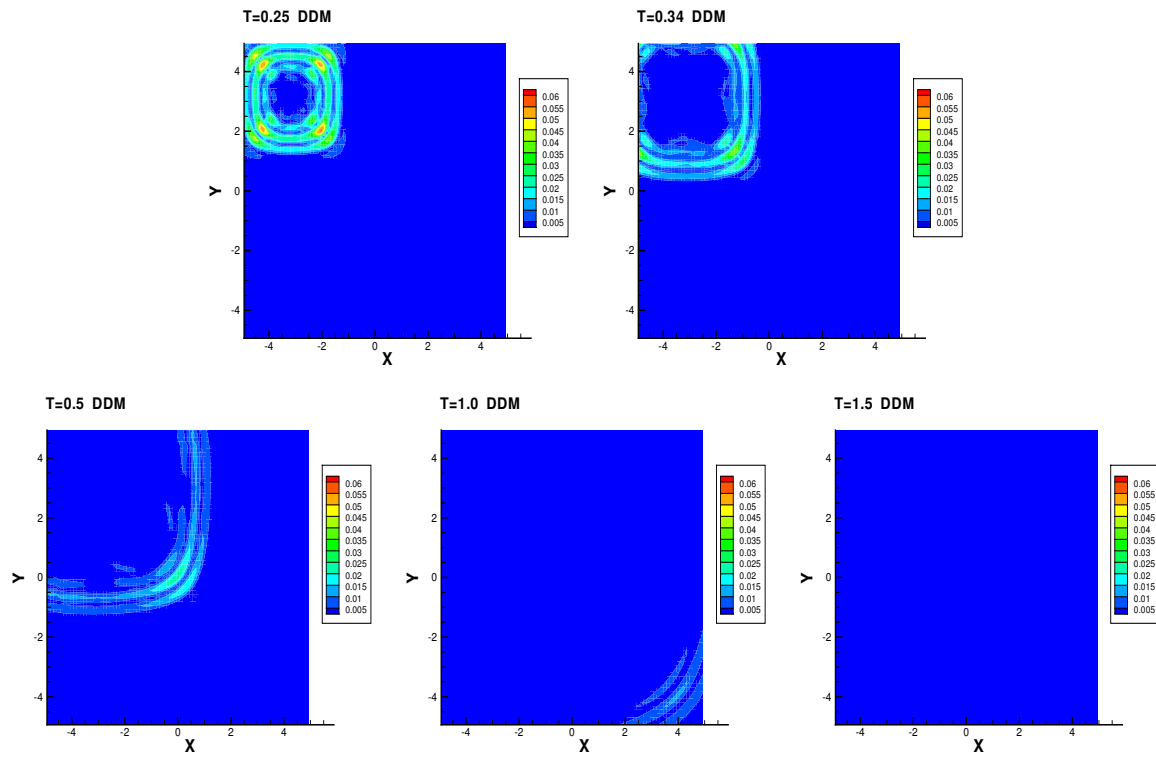


Figure 5.15: Snapshots of the velocity module at different times (by the DDM model): DG P^1 with 80×80 cells.